Three-dimensional magnetotelluric modelling of the Lalor volcanogenic massive-sulfide deposit, Manitoba

S.M. Ansari[1*], E.M. Schetselaar[1], and J.A. Craven[1]

Ansari, S.M., Schetselaar, E.M., and Craven, J.A., 2022. Three-dimensional magnetotelluric modelling of the Lalor volcanogenic massive-sulfide deposit, Manitoba; in *Targeted Geoscience Initiative 5: volcanic- and sediment-hosted massive-sulfide deposit genesis and exploration methods, (ed.) J.M. Peter and M.G. Gadd; Geological Survey of Canada, Bulletin 617, p. 313–327. https://doi.org/10.4095/328003*

Abstract: Unconstrained magnetotelluric inversion commonly produces insufficient inherent resolution to image ore-system fluid pathways that were structurally thinned during post-emplacement tectonic activity. To improve the resolution in these complex environments, we synthesized the 3-D magnetotelluric (MT) response for geologically realistic models using a finite-element–based forward-modelling tool with unstructured meshes and applied it to the Lalor volcanogenic massive-sulfide deposit in the Snow Lake mining camp, Manitoba. This new tool is based on mapping interpolated or simulated resistivity values from wireline logs onto unstructured tetrahedral meshes to reflect, with the help of 3-D models obtained from lithostratigraphic and lithofacies drillhole logs, the complexity of the host-rock geological structure.

The resulting stochastic model provides a more realistic representation of the heterogeneous spatial distribution of the electric resistivity values around the massive, stringer, and disseminated sulfide ore zones. Both models were combined into one seamless tetrahedral mesh of the resistivity field. To capture the complex resistivity distribution in the geophysical forward model, a finite-element code was developed. Comparative analyses of the forward models with MT data acquired at the Earth's surface show a reasonable agreement that explains the regional variations associated with the host rock geological structure and detects the local anomalies associated with the MT response of the ore zones.

Résumé : La résolution inhérente de l'imagerie produite par l'inversion sans contrainte des données magnétotelluriques (MT) est généralement insuffisante pour figurer les voies de circulation des fluides dans les systèmes minéralisés ayant été amincis structuralement par une activité tectonique postérieure à la mise en place de la minéralisation. Afin d'obtenir une meilleure résolution dans ces environnements complexes, nous avons synthétisé la réponse magnétotellurique en 3D de modèles géologiques réalistes en employant un outil de modélisation prévisionnelle par éléments finis appliqué à une grille non structurée et l'avons mis à l'épreuve au gisement de sulfures massifs volcanogènes de Lalor dans le camp minier de Snow Lake, au Manitoba. Ce nouvel outil repose sur la cartographie des valeurs de résistivité interpolées ou simulées tirées de diagraphies par câble et transposées dans une grille non structurée à mailles tétraédriques afin de refléter, avec le soutien de modèles 3D tirés des descriptions lithostratigraphiques et faciologiques de trous de forage, la complexité de la structure géologique des roches hôtes.

Le modèle stochastique qui en résulte fournit une représentation plus réaliste de la distribution spatiale hétérogène des valeurs de résistivité électrique autour des zones de sulfures massifs, filoniens et disséminés. Les deux modèles ont été combinés sur une grille à mailles tétraédriques continue du champ de résistivité. Afin de capturer la distribution complexe de la résistivité dans un modèle géophysique prévisionnel, un code d'éléments finis a été élaboré. Les analyses comparatives des modèles prévisionnels avec les données MT acquises à la surface de la Terre montrent une concordance raisonnable qui permet d'expliquer les variations régionales associées à la structure géologique des roches hôtes et de détecter les anomalies locales associées à la réponse MT des zones minéralisées.

[1]Geological Survey of Canada, 601 Booth Street, Ottawa, Ontario K1A 0E8
*Corresponding author: S.M. Ansari (email: seyedmasoud.ansari@nrcan-rncan.gc.ca)

INTRODUCTION

A more reliable understanding of geophysical data requires expanding forward-modelling schemes to incorporate models that capture a more realistic representation of the variation in physical properties that reflects the geological complexity and lithostratigraphic architecture of the subsurface. This work focuses on the incorporation of detailed variations in physical properties obtained from stochastic simulations of electrical resistivities within lithostratigraphic units. These realistic models can be used as input for geophysical modelling algorithms to test the success of different survey layouts and to investigate if the geometric complexities of the physical property distributions can be observed in the electromagnetic (EM) signal recorded on the Earth's surface. Here we consider the magnetotelluric (MT) method (and the audio-magnetotelluric (AMT) method, its audio frequency band extension), a geophysical technique that provides a measure of naturally varying electromagnetic signals that result from geomagnetic fields and telluric currents interacting with conductive Earth materials (Chave and Jones, 2012). Magnetotelluric response is currently understood mostly for simple models, such as a (dipping) rectangular prism buried in a homogeneous or layered background, and overlain by a nontopographic (e.g. a flat horizontal surface) overburden (e.g. Kalscheuer et al., 2018), or some elongated uniform bodies that are used to represent massive-sulfide deposits (e.g. Balch, 1999). These are unrealistic models that also fail because a constant physical property is chosen for the prismatic or polygonal object in its entirety; this does not capture the structural complexity of mineral deposits with varying distributions of alteration and ore minerals.

We aim to reproduce the geometry of any complex-shaped object, including lithostratigraphic units and faults, using unstructured meshes that conform exactly to all geometries such as topography variations, curvilinear-shaped geological bodies, and sharp interfaces. Unstructured mesh here is defined as a tessellation of the 3-D space by simple tetrahedral elements distributed in an irregular pattern. These meshes provide significant computational benefits and numerical accuracy through local refinement. The generation of an unstructured (i.e. tetrahedral) mesh that is suitable for numerical modelling of electromagnetic (EM) problems must be constructed in a sealed surface model (needed as input for the meshing programs) with all the lithostratigraphic boundaries properly welded at the contact lines. By definition, a sealed model is one with no gaps and holes, and with no node-edge discontinuities between grid cells.

Several workflows for building 'sealed models' — completely partitioned volumetric models consisting of non-overlapping tetrahedrons whose unions equal the modelled volume — from surface-based geological data have been presented during the past decade (e.g. Zehner et al., 2015; Lelièvre et al., 2018); these workflows vary based on the numerical goals, mesh quality, and modeller's effort and control over the procedure. We devised a semi-automatic routine using a combination of geomodelling software — structural knowledge universal approach (SKUA; Gocad-skua® of Paradigm (2014)), model manipulation and conversion tools (FacetModeller of Lelièvre et al. (2018), and RINGMesh of Pellerin et al. (2017), respectively), and a tetrahedral meshing library (TetGen of Si (2014)) — to construct a volumetric tetrahedral mesh that is suitable for our physical-property simulation and numerical-modelling needs. The projection of the geophysical modelling problem onto a meshed domain requires the use of approximate numerical methods. Here, we discretized the relevant partial differential equations (PDEs) using a finite-element (FE) method that best conforms to the irregularity of the unstructured mesh (Ansari and Farquharson, 2014). The FE method approximates the functions in the integral terms of the relevant variational problem that is formed after minimizing the PDE of electromagnetic diffusion using some basis functions (Jin, 2014). The basis functions in our work are designed to meet the physical boundary conditions (i.e. continuity [discontinuity] of the tangential [normal] component of the electric field), across the interelement boundaries of distinct resistivities in the mesh. The product of the FE discretization is a linearized matrix form of the considered PDE. Subject to enforcing the appropriate boundary conditions for the MT fields here, this system is to be solved for the unknown fields (i.e. vector and scalar potentials).

Due to a decline in the discovery of near-surface ore deposits and the limitations of controlled-source EM methods, the MT method has gained popularity for exploring deeper targets such as deeply buried VMS deposits (e.g. Zhang and Chouteau, 1992). The MT signal is sensitive to the high electrical conductivity of massive and stringer sulfide mineralization in the sulfide ore zones, and also to the relatively weaker conductivity of disseminated sulfide minerals in the host rock and alteration zones. Despite a great depth of mineralization (≥600 m deep) in the form of narrow ore lenses at the Lalor volcanogenic massive-sulfide (VMS) deposit, the high abundance of the sulfide minerals gives rise to a sharp conductivity contrast and produces a detectable MT response.

The limited available studies on the application of AMT modelling for realistic models to delineate deeply buried mineral deposits are restricted to investigating the dimensions and conductivities of composite mineralized zones, typically by considering simple-shaped objects for ore surrounded by a background/layered half-space, or tabular-shaped bodies used to represent the disseminated (alteration) zone (e.g. Zhang and Chouteau, 1992; Livelybrooks et al., 1996). The detectability in this context was justified by the role of current channelling effects from the surrounding rocks of the alteration zone; however, this phenomenon has not yet been quantified for a realistic exploration scenario. Legault et al. (2015) demonstrated the detectability of the Lalor VMS deposit using the inversion of z-axis tipper EM (ZTEM) data and produced an image of the anomaly extending to a depth of 1.5 km. This anomaly was also detected in the time-domain EM study of Hodges et al. (2016), as were multiple plate-like conductors around the orebodies to constrain the conductive sulfide-bearing zones of the hanging-wall structures. In a recent study at Lalor, Yang et al. (2019) demonstrated the importance of the *a priori* model for the ZTEM data inversion in imaging the deposit and its lateral extensions; the final model for interpretation was, however, chosen by performing inversions for a number of trial conductivities assigned to homogeneous background models. In contrast to these traditional methods of analyses, which are limited to placing simple prismatic bodies in a homogeneous or layered background, we make use of geostatistical estimation from wireline resistivity logs by merging them into unstructured meshes to respect, with the aid of 3-D models obtained from lithostratigraphic and lithofacies drillhole logs, the complexity and heterogeneity of the mineral deposit and the host rock geological structure.

After briefly reviewing the geological setting of the Lalor VMS deposit, we discuss the workflow of constructing a sealed 3-D geological model from lithostratigraphic units meshed with tetrahedral cells and the process of assigning electrical resistivities to each cell in this mesh. In preparation for synthetically modelling the MT response of this model, we discuss the process of developing a forward modelling tool. For the Lalor model, we have included an analysis of the residuals of the forward model for the MT impedances between the simulated data and the survey field data. We present our detailed investigation of how the inductive and galvanic components of the MT response contribute to forming the total current flow that energizes the sulfide deposit of the Lalor mine.

GEOLOGICAL SETTING

The Lalor VMS deposit is hosted by a sequence of volcanic and volcaniclastic rocks of the Snow Lake arc assemblage in the eastern Flin Flon greenstone belt (Bailes et al., 2016). The arc assemblage section is greater than 6 km thick, comprises three volcanic sequences, and is affected by at least four episodes of deformation (Galley et al., 1993). Figure 1 shows a southwest-northeast-oriented cross-section of the Snow Lake mining camp (*modified from* Schetselaar et al., 2017). The Chisel sequence is subdivided into lower and upper subsequences corresponding to the footwall and hanging wall, respectively, of the mineralized horizon. The deposit is hosted in the lower Chisel sequence and comprises a number of mineralized zones that extend at depths between 570 and 1160 m. The ore lenses are thin (averaging 12 m wide) and are of varying size and grade. The gold-rich zones of the deposit are composed of sulfide stringer vein mineralization. The extension of the gold-copper mineralization in the deeper part of the deposit remains an open exploration target to investigate. A large hydrothermal alteration system in the footwall of the VMS deposit is associated with the emplacement of the Richards subvolcanic intrusion. This intrusion is considered to be the probable heat source that drove hydrothermal circulation that formed the Lalor deposit (Bailes et al., 2016).

PHYSICAL PROPERTY MODEL CONSTRUCTION FROM LITHOSTRATIGRAPHIC DATA

The primary geological data include surfaces of lithostratigraphic contacts (e.g. between units depicted in Fig. 1) built using drillhole markers and surface-mapped contacts. We used these data as input for the structure and stratigraphy (SnS) platform of SKUA to form a number of wireframed triangulated surfaces. After introducing horizons passing through the contact surfaces, SKUA built a chronostratigraphic column bounded by a voxet. The SKUA then computed the volume of interest and a surface meshed domain resampled with triangles so that all units are properly stitched at the intersecting contact lines (Fig. 2a). To further process this model, all the nodes and triangular elements were extracted using the RINGMesh platform (Pellerin et al., 2017) and then imported into the FacetModeller software (Lelièvre et al., 2018) to extend the model domain to exceed padding regions required for numerical correctness of the subsequent forward simulation. The 3-D volumetric mesh was then produced using TetGen (*see* Fig. 2b for a cross-section from the centre of the mesh). We refer to this as the lithostratigraphic-homogeneous model (model S1).

We used two methods to populate the grid model with relevant physical properties. We assigned the resistivity values to mesh cells based on a) the average lithostratigraphic units (referred to as lithostratigraphic-homogeneous, or model S1), and b) variable resistivity using sequential Gaussian simulation (SGS) over the interpolation of 15 lithofacies (referred to as lithofacies-stratified heterogeneous, or model S2). The method of Sequential Gaussian simulation is a stochastic realization that maps resistivities into grid cells by repeatedly extracting random samples from probability distributions of kriged (measures of Gaussian process) resistivity values. Within model S1, seven lithostratigraphic units (shown in Fig. 2a and Table 1) are classified with mean resistivities according to the camp-scale geological outcrop map and the corresponding drill core markers, with mean resistivities then queried from the wireline resistivity log measurements. Table 1 shows the average resistivity values calculated for each lithostratigraphic unit; the regions forming the hanging wall of the model (regions 1–5 in Fig. 2a) are relatively more resistive than the footwall units (regions 6 and 7 in Fig. 2a).

Model S2 maps the lithofacies classes that occur within each of the seven lithostratigraphic units and quantifies the relevant resistivity variations. This is done in three major steps: 1) construction of a curvilinear grid using lithostratigraphic units, 2) categorical kriging of lithofacies, and 3) stratified SGS of resistivity in each lithofacies class conditioned on the resistivity log data (Schetselaar et al., 2017). The lithofacies include mafic to felsic, fine- and coarse-grained, volcanic and volcaniclastic rocks with resistivities

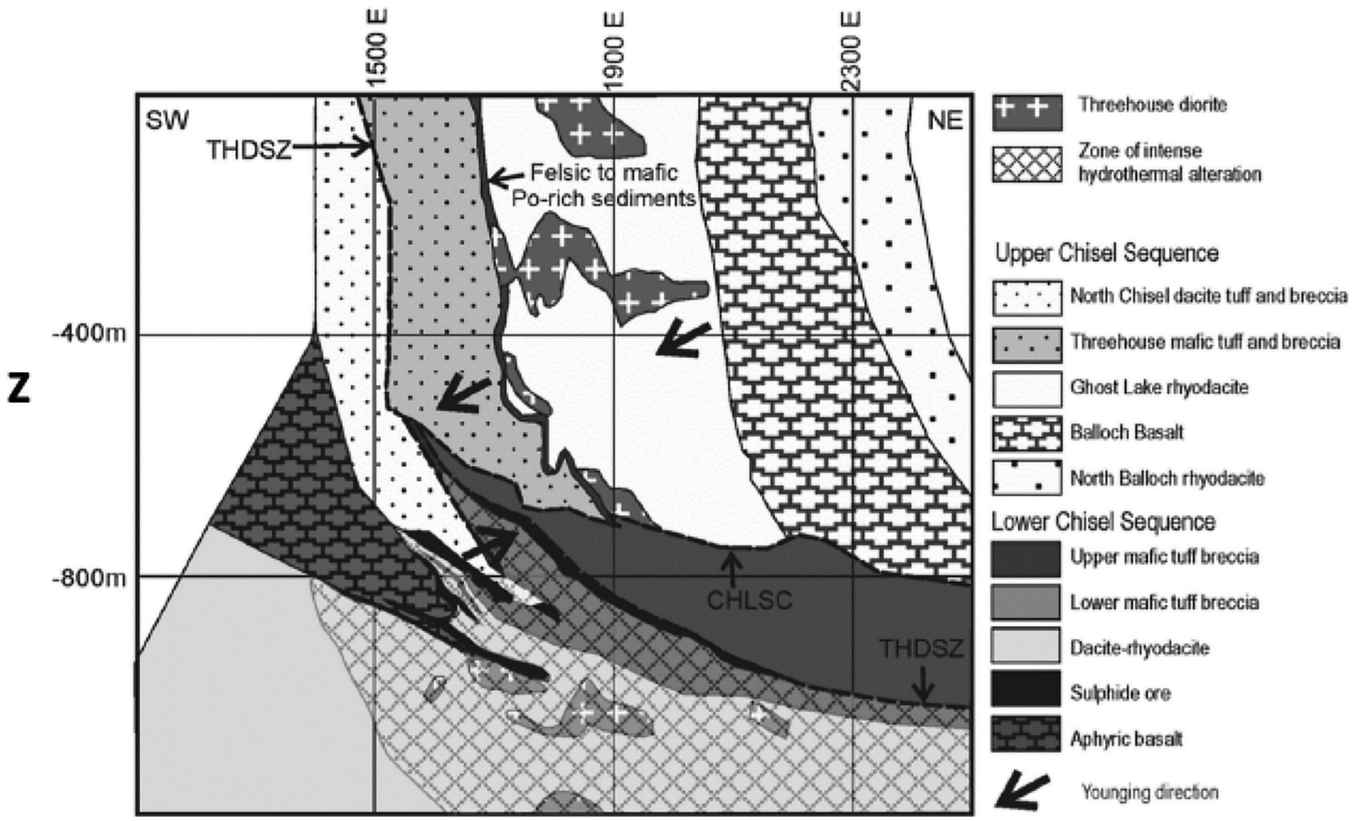

Figure 1. Southwest-northeast cross-section of the Lalor VMS deposit showing the Chisel-Lalor structural contact (CHLSC) and Threehouse ductile shear zone (THDSZ; *modified from* Schetselaar et al., 2017).

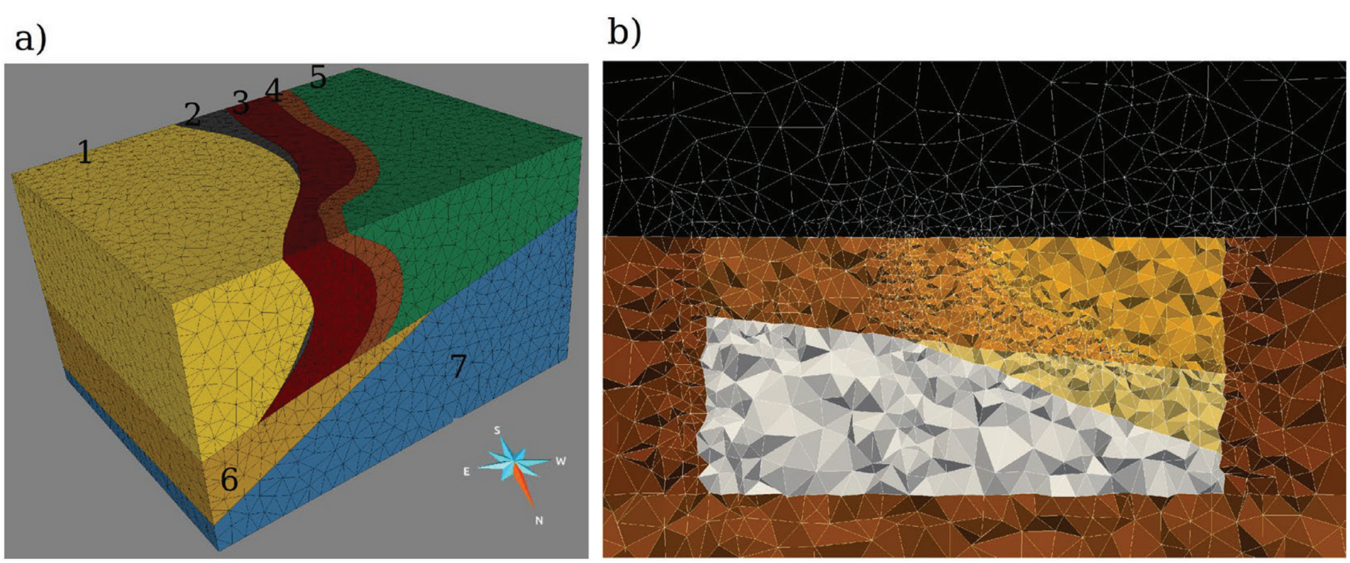

Figure 2. a) Illustration of the sealed (watertight) surface mesh produced in GOCAD® by Paradigm (Paradigm, 2014) that shows the regions between units at the Lalor volcanogenic massive-sulfide deposit. The numbers correspond to the regions in Table 1. The region of interest is marked by a rectangle on the Earth's surface; **b)** a magnified cross-section view of the tetrahedral mesh through the region of interest and surroundings, produced for the block model S1.

Table 1. Average resistivity values for the generalized lithostratigraphic units and the sulfide ore lenses of the Lalor 3-D geological model.

Region; name	Rock types	Mean resistivity (Ω-m)
1; Above Balloch	Intermediate volcaniclastic rocks	8912
2; Balloch	Basalt	2884
3; Ghost Lake	Rhyodacite	3311
4; Threehouse	Mafic volcaniclastic rocks	5011
5; Chisel	Intermediate volcaniclastic rocks	7413
6; Lower Chisel sequence	Upper mafic volcaniclastic rocks	338
7; Lower Chisel sequence	Lower mafic tuff breccia, aphyric basalt, dacite-rhyodacite	87
Sulfide ore	Mafic rocks	Variable

Regions correspond to the units numbered in Figure 2.

ranging from 1000 to 10 000 Ω-m. Intermediate volcanic rocks, coarse-grained mafic volcaniclastic rocks, and argillite show bimodal resistivity distributions because they host disseminated sulfide minerals. Using conditional probability distribution from the kriging mean, the SGS method randomly picks sample resistivity values from the distributions and assigns them into the curvilinear grid cells. Figure 3a shows one of the many resistivity models produced among multiple stochastic realizations. The resistivity values from this curvilinear grid are projected onto our tetrahedral mesh using the inverse distance weighting (IDW) strategy (Shepard, 1968). To capture resistivity-conductivity stratification associated with the entire region of ore zone, the mesh was locally refined by inserting a cloud of nodes within the footwall of model S1 and along the path of the vertical and dipping resistivity logs. Using a 500 m search radius and an exponent factor for the distance weighting of 10, the IDW method assigned an average resistivity to each node in the tetrahedral mesh. These nodal resistivities were then interpolated to the centre of cells in the mesh. Views of the final product demonstrate the bedding and spatial lithostratigraphic structure of the footwall zone; Figure 3b and 3d show two selected cross sections through the model. Using the electrical resistivity values assigned to each mesh cell, an MT forward-modelling tool was developed that calculates the fields, currents, and response functions of the considered model. It is noteworthy to mention that the mesh is also refined at the observation locations on the surface (Fig. 3c). This is very important for calculating accurate fields and the subsequent MT responses at each location. Local refinement within the computational domain at depth allowed us to merge as much resistivity information as possible from the discrete SGS data into the meshed physical property model.

FINITE-ELEMENT SIMULATION OF THE MAGNETOTELLURIC RESPONSE

We only mention the salient features of our forward-modelling method here; a detailed description of this development is presented in Ansari et al. (2020). The modelling scheme is based on solving a system of PDEs consisting of the Helmholtz diffusion equation — with the electric field decomposed as $\boldsymbol{E} = -i\omega\boldsymbol{A} - \nabla\phi$ — and the Coulomb gauge condition:

$$\nabla \times \nabla \times \boldsymbol{A} + (i\omega\mu\sigma - \omega^2\mu\epsilon)\boldsymbol{A} + (\mu\sigma + i\omega\mu\epsilon)\nabla\phi = \boldsymbol{0} \quad (1)$$

$$\nabla \cdot \boldsymbol{A} = \boldsymbol{0} \quad (2)$$

Here ∇ represents the gradient operator, and ω, μ, and ϵ are angular frequency (radians), magnetic permeability (H/m), and electric permittivity (F/m), respectively. $\boldsymbol{A}$ and ϕ are the vector and scalar potentials, respectively. The parameter σ is the electric conductivity (S/m). The system consisting of equations 1 and 2 was solved subject to imposing appropriate boundary conditions for $\boldsymbol{A}$ and ϕ. We enforced the conditions on the tangential components of the vector potential and the value of the scalar potential on the outer 2-D boundaries of the mesh. This initially required the implementation of 1-D boundary conditions on the corners of the sides of the 3-D domain. For this, the 1-D variant of equation 1 is solved considering a zero scalar potential because no current flows across the changes in conductivity between layers in the z-direction for the 1-D case. The solutions from the 1-D problem then served as inputs to constrain the boundary conditions of the 2-D problem on the sides of the 3-D domain. The 2-D variant of equation 1 is solved for each MT polarization mode: on the x-z side boundaries for the x-polarization and on the y-z side boundaries for the y-polarization. We also enforced constant horizontal magnetic fields to constrain the field at the topmost boundary of the mesh that corresponds to the magnetosphere source. After implementation of the 2-D solutions, the 3-D $\boldsymbol{A}$-ϕ problem was solved using the 2-D solutions on the side boundaries. Here the system of equations for the 1-D, 2-D, and 3-D problems were discretized using the finite-element approach. In particular, and using the FE method, the problem of solving the exact-form PDEs formulated above was replaced by solving the weak-form approximate equations in an average sense over the considered physical domain (Jin, 2014). This was done by orthogonalizing the $\boldsymbol{A}$-ϕ system with the relevant weight functions and then approximating these potentials using the appropriate basis functions over tetrahedral cells. This resulted in a discretized system of equations that must be solved for the approximate vector ($\tilde{\boldsymbol{A}}$) and scalar ($\tilde{\varphi}$) potentials:

$$\begin{pmatrix} S + i\omega\mu\boldsymbol{M} - \omega^2\mu\mathbf{N} & \mu\boldsymbol{F} + i\omega\mu\boldsymbol{G} \\ \boldsymbol{H} & \mathbf{0} \end{pmatrix} \begin{pmatrix} \widetilde{A_e} \\ \widetilde{\varphi_n} \end{pmatrix} = \begin{pmatrix} S_{r_{air}} + S_{r_{sides}}^{A,2D} \\ S_{r_{sides}}^{\varphi,2D} \end{pmatrix} \quad (3)$$

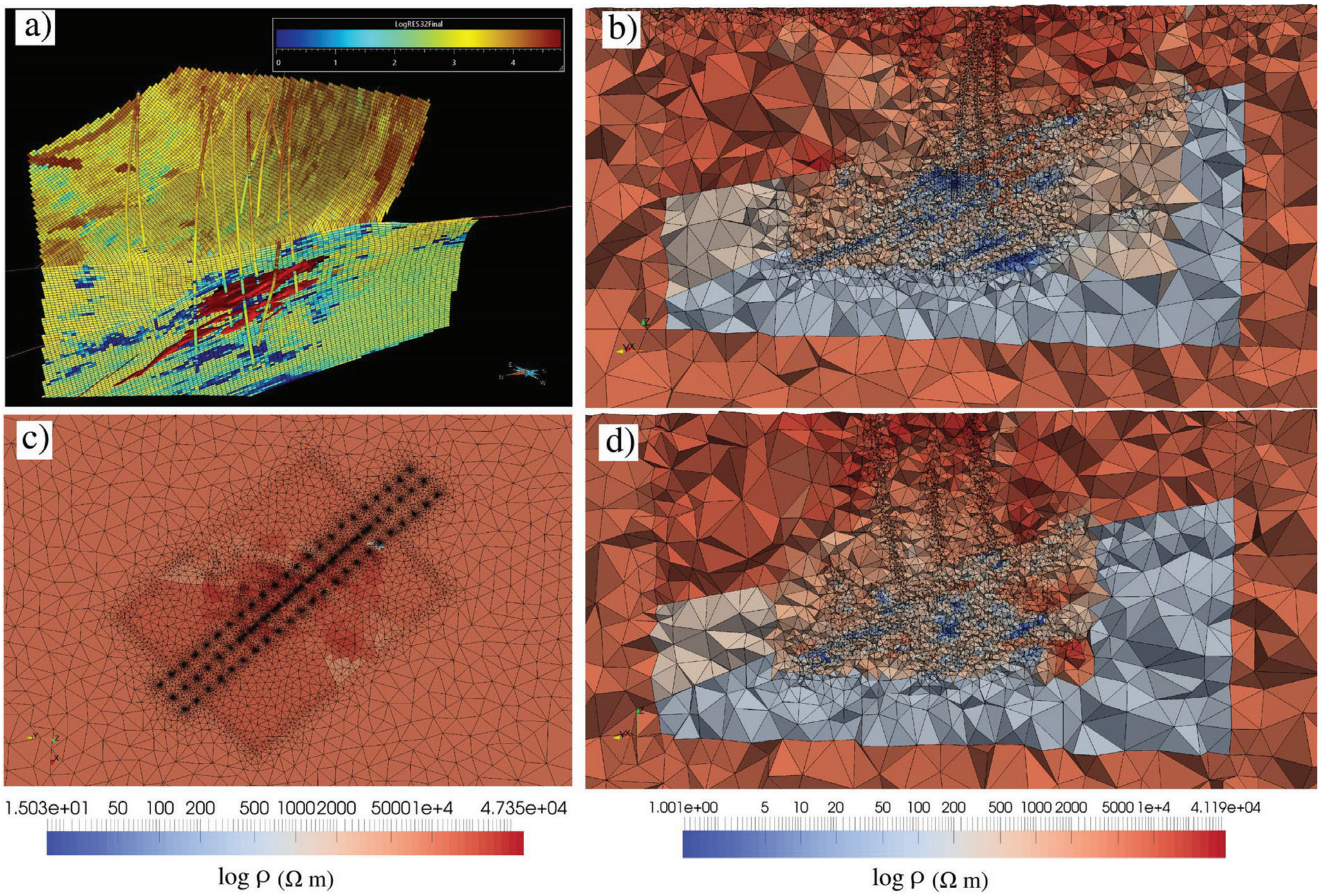

Figure 3. Process of populating the mesh with resistivities: **a)** cross-section showing a sequential Gaussian simulation realization on a curvilinear grid; the wireline logs and ore lenses are shown in red; **b)** and **d)** magnified cross-section views of the unstructured mesh showing the resistivity distributions in the central part of the model after applying inverse distance weighting and linear interpolation schemes for nodal resistivities (model S2); **c)** plan view showing the refinement along three profiles of observations on the Earth's surface.

The bold variables (***S***, ***M***, ***H***, ***N***, ***F***, ***G***) are the inner product integrals associated with FE functionals derived for terms on the left-hand side of equations 1 and 2. The terms on the right-hand side of equation 3 come from the imposition of the boundary conditions on the side and top boundaries of the mesh discussed above. The solution of this system gave the vector potential ($\tilde{\boldsymbol{A}}_e$) for edges and scalar ($\widetilde{\varphi_\eta}$) potential for nodes. The direct solver MUMPS (multifrontal massively parallel solver; Amestoy et al., 2001, 2006) was used to efficiently solve the system of equations. The MUMPS software uses OpenMP, a multiprocessing application programming interface, to perform the calculation in a multi-threaded manner that uses all the processor units in the computer. The pre-solution components of the numerical codes compute the FE inner-product integrals of equation 3. Using the approximate vector and scalar potentials we calculated the electric and magnetic fields and then the MT response functions including impedances, transfer functions (tipper vectors), apparent resistivities, and phases.

MAGNETOTELLURIC RESPONSE OF THE LALOR DEPOSIT

The MT response of the Lalor models, including the lithostratigraphic-homogeneous (S1) and the lithofacies-stratified heterogeneous (S2) models, is investigated for a range of frequencies. Figures 4–6 compare the impedances produced from synthetic calculations of models S1 and S2 to those of survey field data. Model S1 data predict only the regional geometry of the units, whereas model S2 data add detailed inhomogeneities thought to come from the structural dismemberment of the ore structure. The residual data are generally near zero for model S2, particularly within the zone where the data of SGS realization is interpolated into the model. For a frequency of 117.20 Hz, the root mean square error (RMSE) between calculated and field data for all observation locations is 18 and 20% for the real and imaginary parts, respectively; the RMSE is reduced to 11 and 16%, respectively, for the observation locations inside the stochastic domain. This is an indication of how well model S2 predicts the field data.

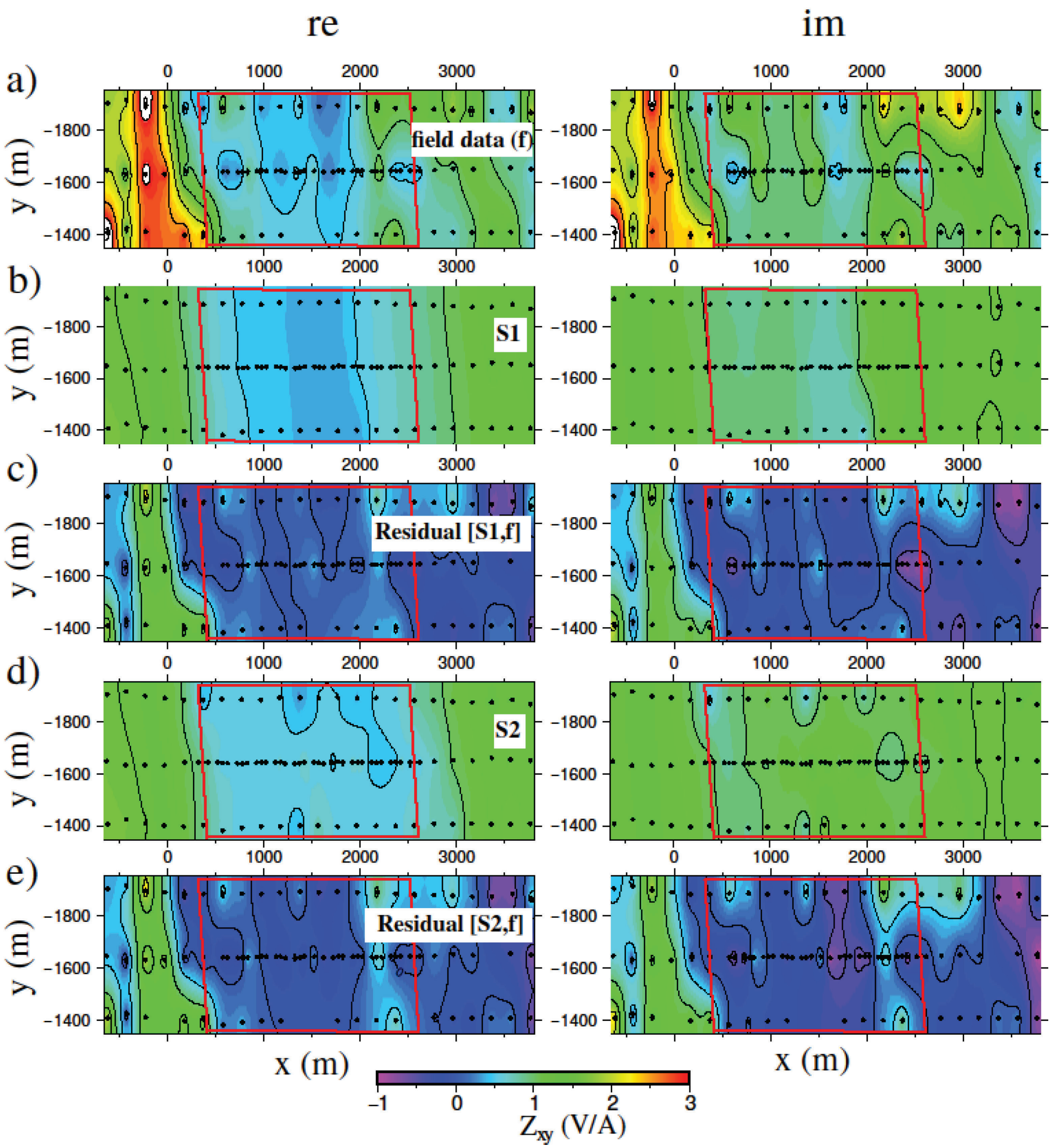

Figure 4. Comparison of the real (re) and imaginary (im) parts of the field and synthesized magnetotelluric impedances (xy components) for the lithostratigraphic-homogeneous (model S1) and lithofacies-stratified heterogeneous (model S2) models of the Lalor volcanogenic massive-sulfide deposit at a frequency of 117.2 Hz: **a)** impedance contours acquired in the field; **b)** impedance response of model S1; **c)** residuals between the synthesized data from model S1 and the field data; **d)** impedance response of model S2; **e)** residuals between synthesized data of model S2 and the field data. The box in red depicts the boundaries of the model with stochastic properties included.

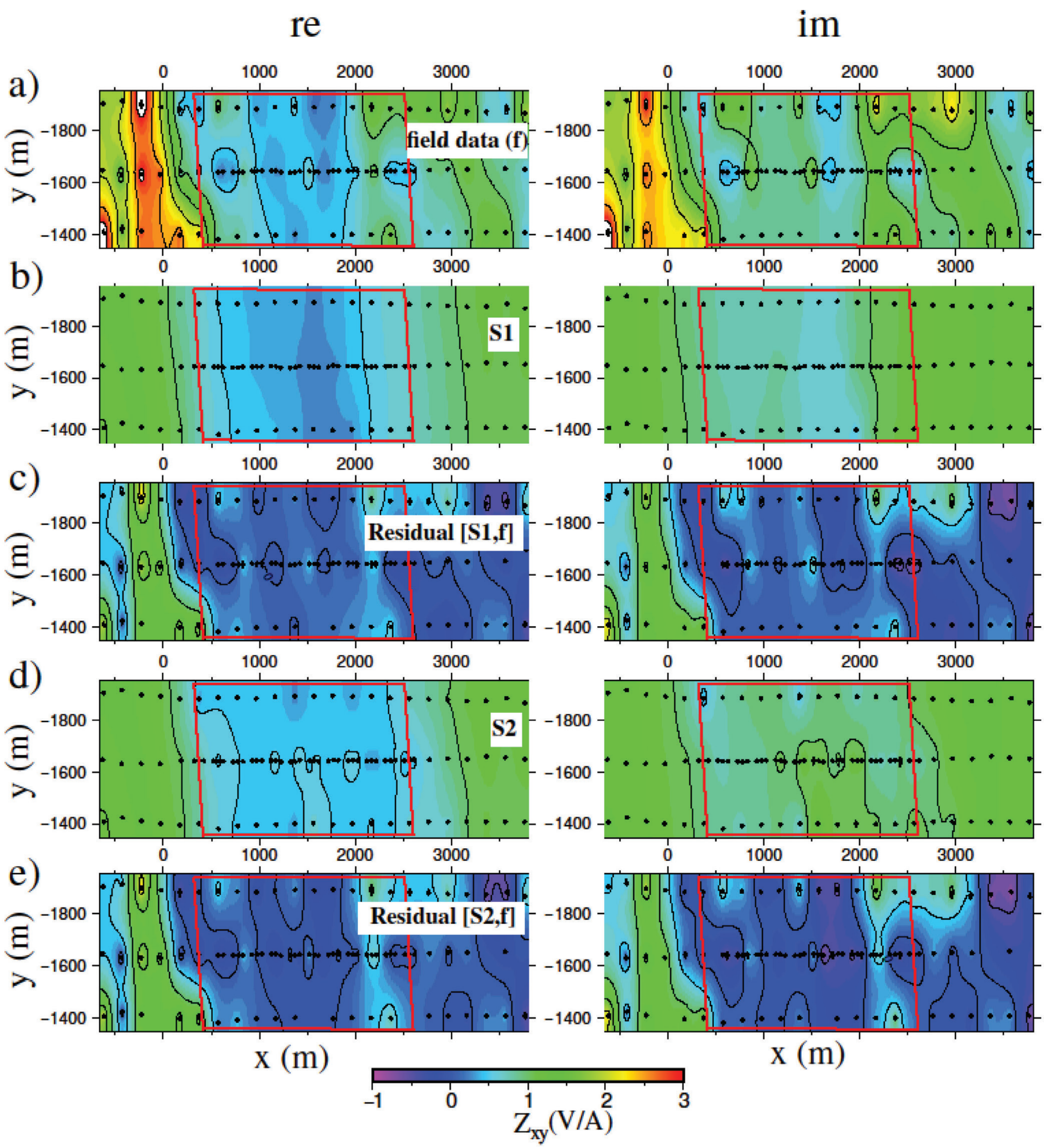

Figure 5. Comparison of the real (re) and imaginary (im) parts of the field and synthesized magnetotelluric impedances (xy components) for the lithostratigraphic-homogeneous (model S1) and lithofacies-stratified heterogeneous (model S2) models of the Lalor volcanogenic massive-sulfide deposit at a frequency of 93.74 Hz: **a)** impedance contours acquired in the field; **b)** impedance response of model S1; **c)** residuals between the synthesized data from model S1 and the field data; **d)** impedance response of model S2; **e)** residuals between synthesized data from model S2 and field data. The box in red depicts the boundaries of the model with stochastic properties included.

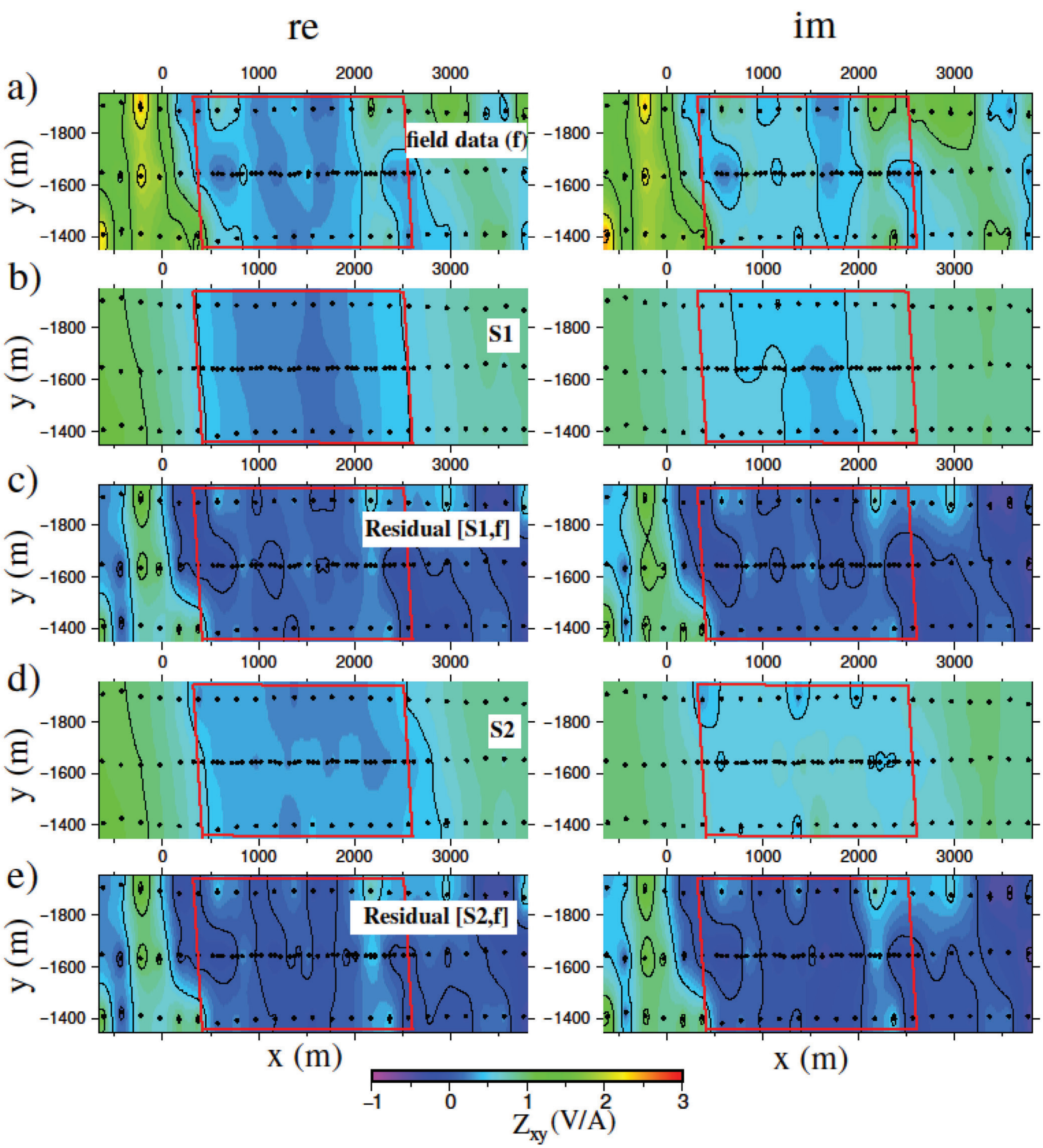

Figure 6. Comparison of the real (re) and imaginary (im) parts of the field and synthesized magnetotelluric impedances (xy components) for the lithostratigraphic-homogeneous (model S1) and lithofacies-stratified heterogeneous (model S2) models of the Lalor volcanogenic massive-sulfide deposit at a frequency of 49.21 Hz: **a)** impedance contours acquired in the field; **b)** impedance response of model S1; **c)** residuals between the synthesized data from model S1 and the field data; **d)** response of model S2; **e)** residuals between synthesized data from model S2 and field data. The box in red depicts the boundaries of the model with stochastic properties included.

To highlight the significance of model S2 we compared survey field MT data pseudosections (for all frequencies) to the synthetic data from models S1 and S2 and to data produced for a model consisting of ore lenses with resistivity of 1 Ω-m buried within a relatively resistive homogeneous background with an average resistivity of 6024 Ω-m). The data for these comparisons are shown in Figures 7–10. We demonstrate here that placing the orebodies only within a half-space of uniform resistivity does not provide a scale of observable MT responses of the ore deposit for impedances, resistivities, and phase data (*see* Fig. 8a, b, and c). In contrast, the data produced from models S1 and S2 enhanced the detectability of the ore deposit by distorting the corresponding MT responses (*see* Fig. 9a, b, and c for S1, and Fig. 10a, b, and c for S2) toward the survey field responses (Fig. 7a, b, and c). Here, the background lithostratigraphic sequence built into model S1 produced an overall decrease in the impedances and resistivities (Fig. 9a and b, respectively), acting similarly to a low-pass filter of the corresponding field data (Fig. 7a and b). The phase data are of particular interest because they provide a qualitative picture of the ore deposit (Fig. 9c) with a maximum of 66° compared to 45° for the background for frequencies greater than 10 Hz. The general orientation of the phase contours reflects the dipping geometry of the background lithostratigraphic units. When perturbed with stochastic resistivities, the model S2 produced impedances and resistivities (Fig. 10a and b, respectively) that better match the data. As with model S1, the overall geometry of the lithostratigraphic sequence dominates model S2 phase data (Fig. 10c), although with minor contributions from the ore deposit inhomogeneities superimposed on the contour lines. This is thought to be caused by enhancement of the current through the relatively conductive footwall units and structures built in the form of inhomogeneities around and within the ore formations.

We demonstrate the current enhancement by visualizing the fields and currents for a vertical section that cuts through the centre of the deposit (Fig. 11). These plots correspond to the average of the x- and y-polarization modes (their absolute values) for two frequencies, as indicated. We demonstrate that induction (E^{ind}_{anom}) as a background field shows a vortex-type behaviour (rotational fields) with peaks that are significantly weaker compared to the galvanic fields (E^{ind}_{anom}). In fact, for the two frequencies shown here, the galvanic part dominantly contributes in forming the total anomalous electric field (E^{tot}_{anom}) through the vertical section. The lower frequency of 3.16 Hz provides a better picture of the entire ore deposit because the relatively larger galvanic field pumps currents (J^{tot}_{anom}), known as footwall feeders, into the ore deposit from the sides and deeper parts of the strata. This phenomenon led to the relatively more energized ore zone with a frequency of 3.16 Hz compared to 117.20 Hz. The inductive and galvanic parts together form the total electric field, and the inductive part (its curl) forms the total magnetic field.

The magnitude and phase of the impedances, however, show sensitivities to different parts of the model at different frequencies. Figure 12 shows the synthesized impedances and phases of the determinant data for sample frequencies of 1313, 117.2, 49.21, and 3.16 Hz. The impedances and phases produced at 1313 Hz are sensitive to the dipping trend and dimensions of the ore formations, whereas the lower frequencies (49.21 and 3.16 Hz) show sensitivity to the relatively larger regional conductivity variations within the deeper parts of the model strata. As anticipated the phase response for the lower frequencies provided little of ore geometry as the peak phase appears within a relatively higher frequency range.

DISCUSSION

We investigated the factors that contribute to the detection of the Lalor VMS deposit using the MT (and AMT) exploration method. In particular, given the relevance of the conductivity contrast between the ore deposit and background host, we explored the importance of the inhomogeneity within the lithostratigraphic units and the existence of deeper conductive feeders in boosting the detectability of the deposit. Novel in-situ estimation of rock resistivities from wireline data merged into our forward-modelling mesh was one of the new achievements of this work. With this realistic resistivity model we demonstrated that phase enhancement over a period ranging from 10 to 10 000 Hz captured the full extent of the ore deposit and its approximate dipping geometry. We also simulated the spatially varying patterns of the survey MT data (shown using impedance and apparent resistivity pseudosections) by incorporating detailed structures associated with the ore inhomogeneities at depth. Considering the dimension and depth of the Lalor deposit we found that the galvanic part of the MT response dominantly contributes to forming the anomalous fields and provides indications of the complexity of the conductive inhomogeneities. The inductive response, attributable to the magnetic field, contributes to a relatively small fraction of the total electric field. These findings can be useful to industry for designing efficient MT surveys that measure the magnetic field at only a selected number of sites across the survey area. The numerical methodology developed here can be applied to ground-level, borehole, and airborne EM methods for a better understanding of the relatively shallower parts of the Lalor deposit.

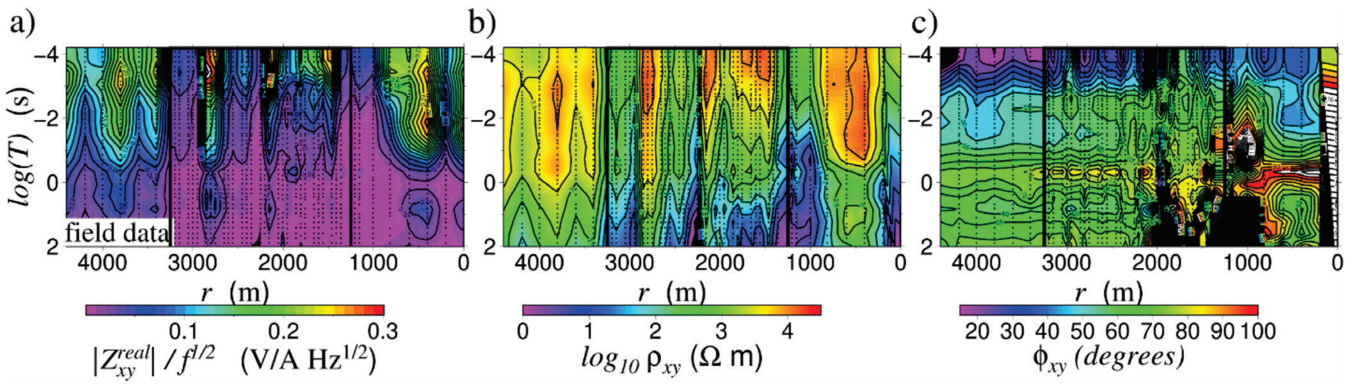

Figure 7. Pseudosections of the magnetotelluric responses for the survey data: **a)** real part of impedance (the xy component), and the corresponding **b)** apparent resistivity and **c)** phase data.

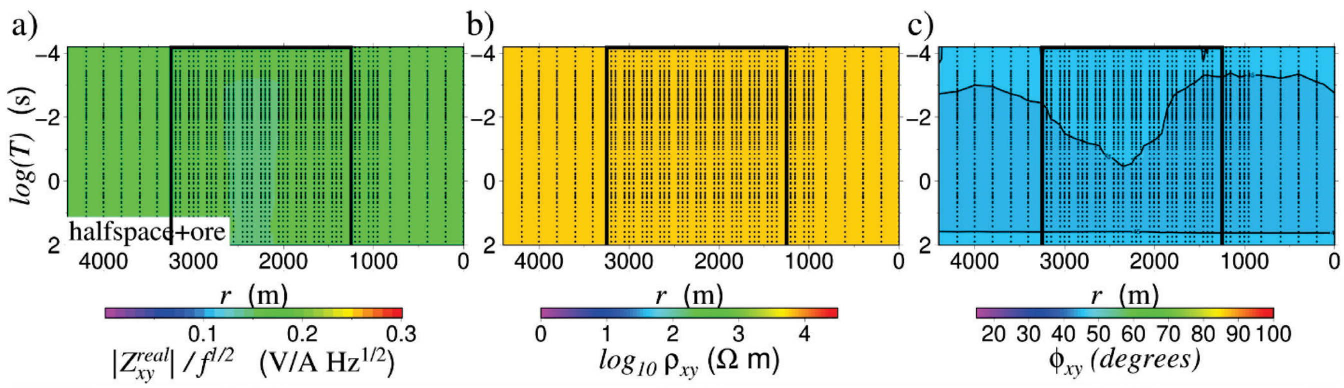

Figure 8. Pseudosections of the magnetotelluric responses for the ore lenses buried in half space: **a)** real part of impedance (the xy component), and the corresponding **b)** apparent resistivity and **c)** phase data.

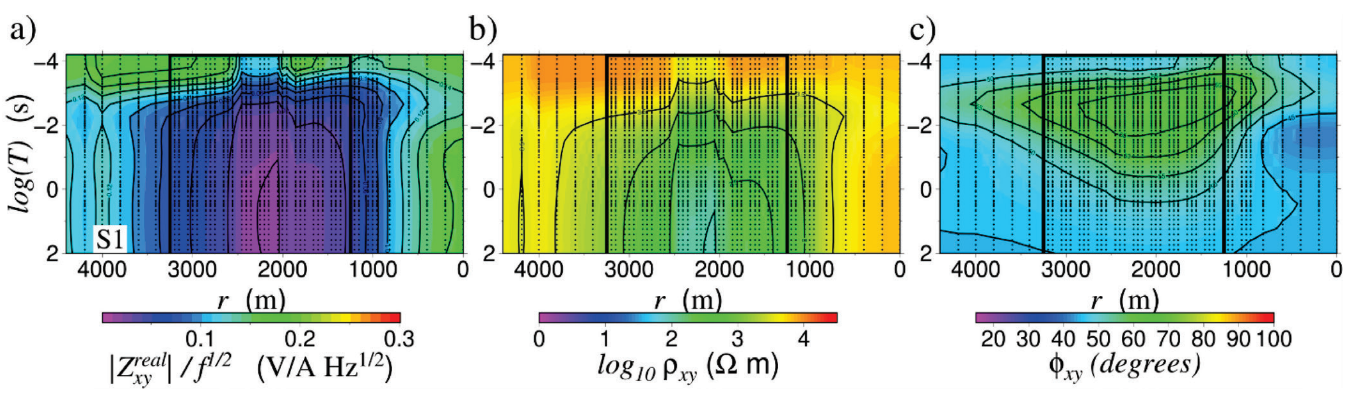

Figure 9. Pseudosections of the magnetotelluric responses for the model S1: **a)** real part of impedance (the xy component), and the corresponding **b)** apparent resistivity and **c)** phase data.

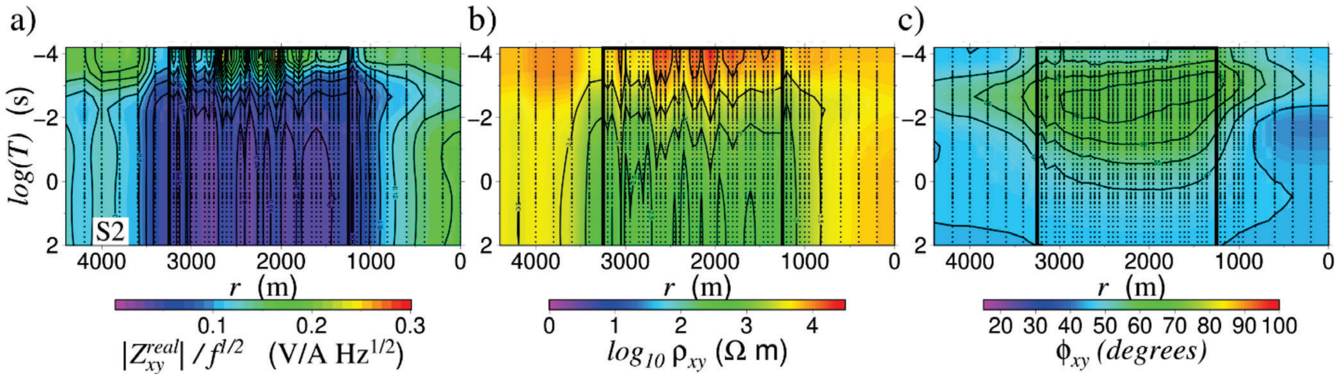

Figure 10. Pseudosections of the magnetotelluric responses for the model S2: **a)** real part of impedance (the xy component), and the corresponding **b)** apparent resistivity and **c)** phase data.

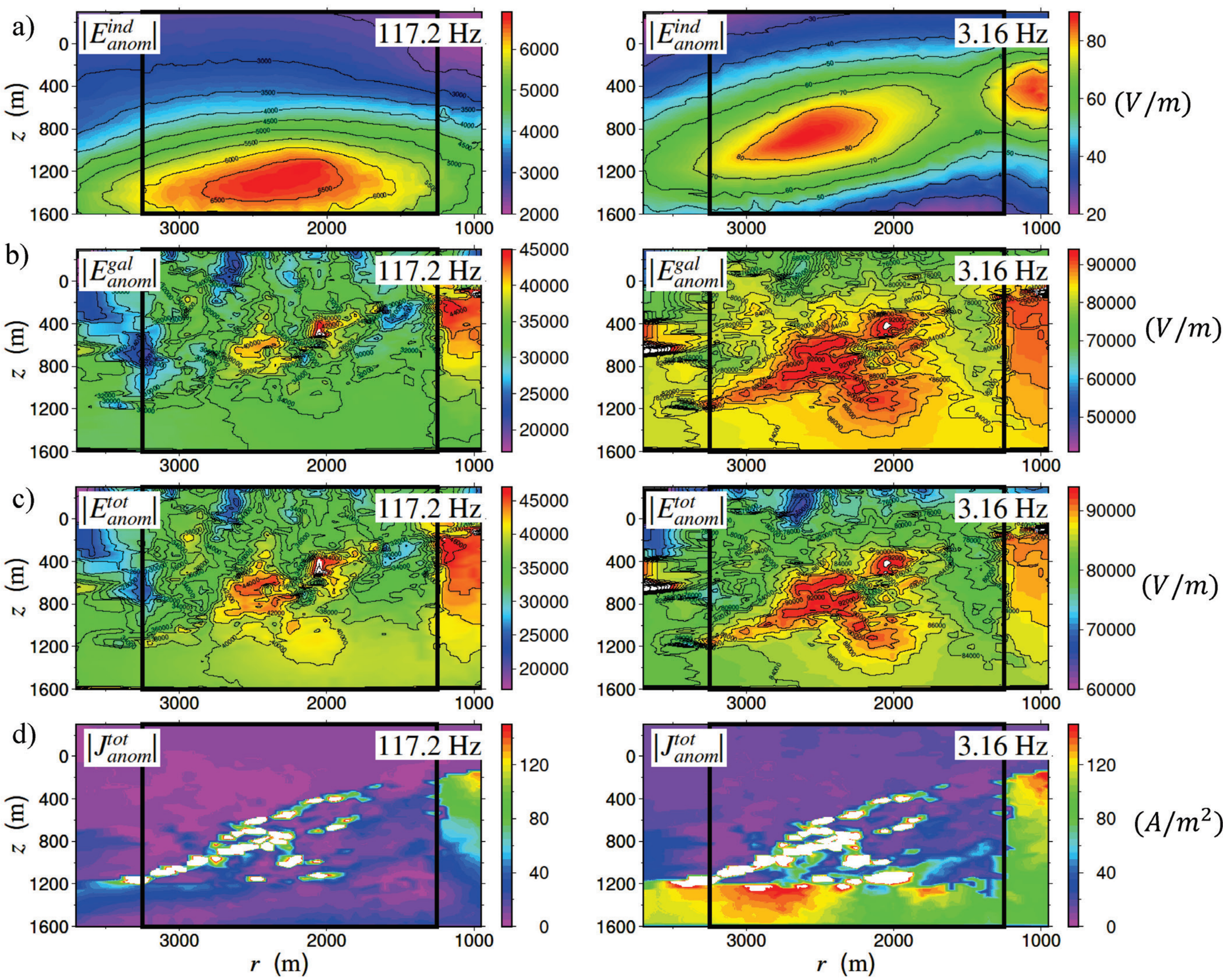

Figure 11. Vertical section of fields and currents for two frequencies through the ore deposit in model S2: **a)** synthetic inductive electric field; **b)** galvanic electric field (in Hz); **c)** total electric field; row **d)** the anomalous current density (background subtracted from total currents)

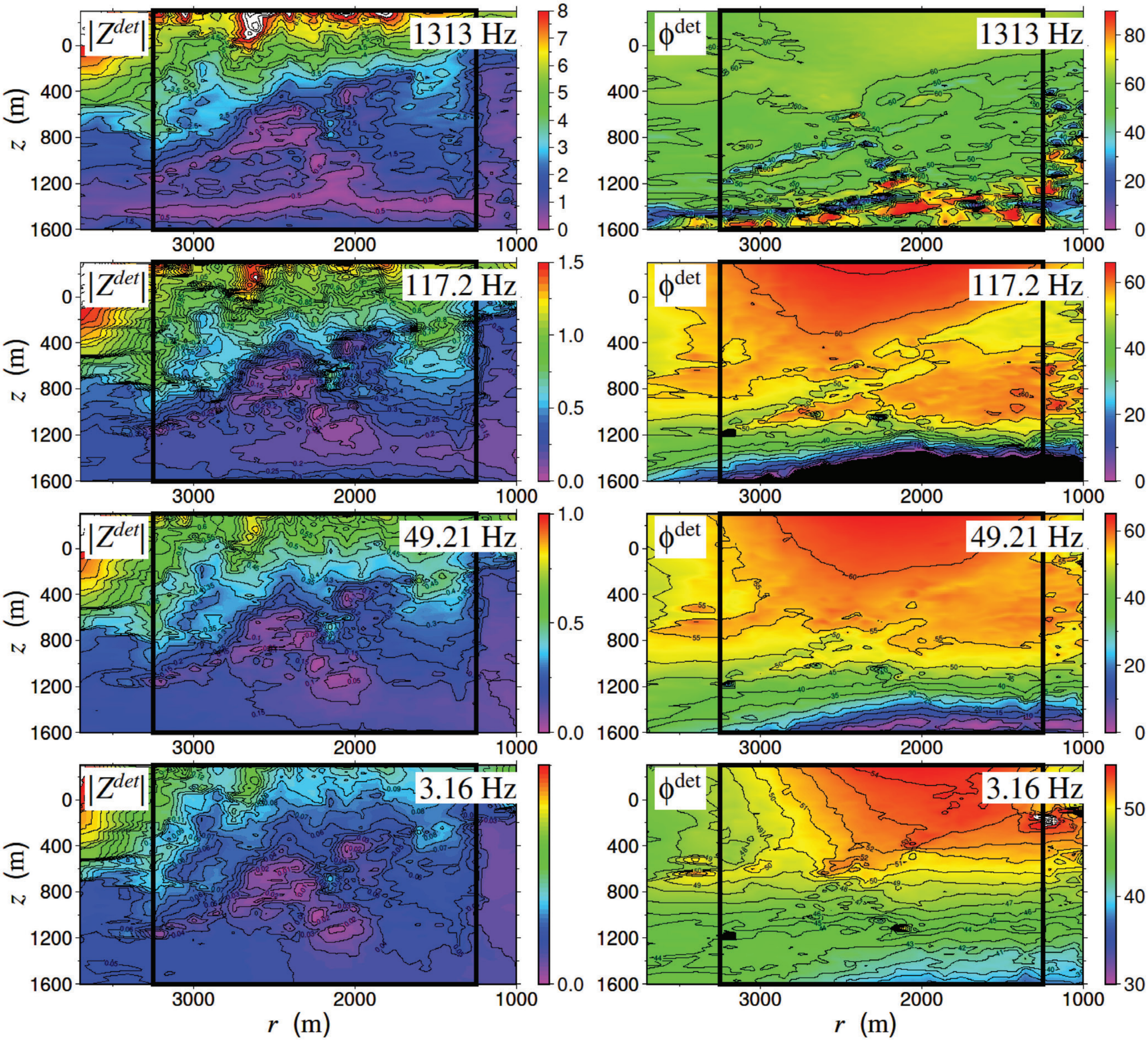

Figure 12. Vertical section through the ore deposit of model S2 showing a) the impedance (left column) and phase (right column) determinant data for four frequencies. The units for impedance and phase are (V/A) and degrees, respectively.

CONCLUSIONS

The purpose of this study was to develop tools to synthesize and analyze the 3-D (audio) MT response of geologically realistic forward models of complex-shaped mineral systems. The originality of this work is associated with the methods we used to populate the model space in conjunction with realistic resistivity variation of a mineral deposit with complex geological structure consisting of massive and stringer ore. Using a combination of SKUA, FacetModeller, RINGMesh, and TetGen, we have developed a semi-automatic process for the construction of an input volumetric meshed model that can be used for realistic MT modelling work. To demonstrate, we applied this process to the Lalor VMS deposit. A sealed, unstructured tetrahedral mesh was generated by compartmentalizing the host rock into major lithostratigraphic units, including massive-sulfide ore zones. By attributing resistivity values to each node, we built a regional 3-D resistivity background model. Using the dense drillhole inputs available in several locations, we calculated more detailed resistivity distributions using categorical kriging of the dominant lithofacies, followed by SGS of the resistivity wireline logs in each lithofacies class. The result was a stochastic model that exhibits a more realistic heterogeneity of the electric resistivity distribution of the massive, stringer, and disseminated sulfide ore zones. The stochastic models were combined into a tetrahedral mesh of the resistivity. We then developed a finite-element code for the MT problem that captures the abovementioned complexity in the model. This algorithm is designed for full, multi-dimensional, natural-EM source fields and calculates the relevant MT responses by solving the potential-variant of the diffusion problem in 3-D. A comparative analysis of the synthetic models with the survey MT data indicates a reasonably acceptable correspondence explaining both the regional and local anomalies associated with the host rock geological structures and local anomalies of the ore zones. A detailed investigation of the inductive and galvanic parts revealed the mechanism through which the MT currents energized the ore zone of the Lalor deposit through galvanically charged fields around relatively conductive ore formations. We also highlighted the importance of relatively conductive alteration zones or a disseminated halo around the ore target in increasing ore detectability. The stochastic resistivity model constructed based on stratified SGS lowered the residuals between measured and modelled MT responses compared to models with homogeneous background resistivities and resistivities averaged over the lithostratigraphic units. Reproducing oscillatory behaviour of the data at different frequencies clearly demonstrates the importance of properly modelling the fractal behaviour of the resistivity distribution in forward modelling of MT data. This work also gives more insight in how to implement inversions by providing guidelines for setting inversion parameters, including assigning suitable error bars to field data coming from small geological features, which may lead to a better interpretation of inversion results.

REFERENCES

Amestoy, P.R., Duff, I.S., Koster, J., and L'Excellent, J.Y., 2001. A fully asynchronous multifrontal solver using distributed dynamic scheduling; SIAM Journal on Matrix Analysis and Applications, v. 23, no. 1, p. 15–41. https://doi.org/10.1137/S0895479899358194

Amestoy, P.R., Guermouche, A., L'Excellent, J.Y., and Pralet, S., 2006. Hybrid scheduling for the parallel solution of linear systems; Parallel Computing, v. 32, no. 2, p. 136–156. https://doi.org/10.1016/j.parco.2005.07.004

Ansari, S.M. and Farquharson, C.G., 2014. 3D finite-element forward modeling of electromagnetic data using vector and scalar potentials and unstructured grids; Geophysics, v. 79, no. 4, p. E149–E165. https://doi.org/10.1190/geo2013-0172.1

Ansari, S.M., Schetselaar, E.M., Craven, J.A., and Farquharson, C.G., 2020. Three-dimensional magnetotelluric numerical simulation of realistic geological models; Geophysics. https://doi.org/10.1190/geo2019-0214.1

Bailes, A.H., Galley, A.G., Paradis, S., and Taylor, B., 2016. Variations in large synvolcanic alteration zones at Snow Lake, Manitoba, Canada, with proximity to associated volcanogenic massive sulphide deposits; Economic Geology, v. 111, no. 4, p. 933–962. https://doi.org/10.2113/econgeo.111.4.933

Balch, S., 1999. Geophysical methods for nickel deposits with examples from Voisey's bay: GAC-MAC Meeting, St. John's, Newfoundland.

Chave, A.D. and Jones, A.G. (ed.), 2012. The magnetotelluric method: theory and practice; Cambridge University Press, Cambridge, United Kingdom, 552 p. https://doi.org/10.1017/CBO9781139020138

Galley, A.G., Bailes, A.H., and Kitzler, G., 1993. Geological setting and hydrothermal evolution of the Chisel Lake and North Chisel Zn-Pb-Cu-Ag-Au massive sulphide deposits, Snow Lake, Manitoba; Exploration and Mining Geology, v. 2, no. 4, p. 271–295.

Hodges, G., Chen, T., and van Buren, R., 2016. HELITEM detects the Lalor VMS deposit; Exploration Geophysics, v. 47, no. 4, p. 285–289. https://doi.org/10.1071/EG16006

Jin, J.M., 2014. The finite element method in electromagnetics, third edition; John Wiley & Sons, Hoboken, New Jersey, 846 p.

Kalscheuer, T., Juhojuntti, N., and Vaittinen, K., 2018. Two-dimensional magnetotelluric modelling of ore deposits: improvements in model constraints by inclusion of borehole measurements; Surveys in Geophysics, v. 39, no. 3, p. 467–507. https://doi.org/10.1007/s10712-017-9454-y

Legault, J.M., Plastow, G., Zhao, S., Bournas, N., Prikhodko, A., and Orta, M., 2015. ZTEM and VTEM airborne EM and magnetic results over the Lalor copper gold volcanogenic massive sulphide deposit region, near Snow Lake, Manitoba; Interpretation, v. 3, no. 2, p. SL83–SL94. https://doi.org/10.1190/INT-2014-0245.1

Lelièvre, P.G., Carter-McAuslan, A.E., Dunham, W.M., J ones, D.J., Nalepa, M., Squires, C.L., Tycholiz, C.J., Vallèe, M.A., and Farquharson, C.G., 2018. FacetModeller: Software for manual creation, manipulation and analysis of 3D surface-based models; SoftwareX, v. 7, p. 41–46. https://doi.org/10.1016/j.softx.2018.02.002

Livelybrooks, D., Mareschal, M., Blais, E., and Smith, T., 1996. Magnetotelluric delineation of the Trillabelle massive sulfide body in Sudbury, Ontario; Geophysics, v. 61, no. 4, 971–986. https://doi.org/10.1190/1.1444046

Paradigm, 2014. GOCAD by Paradigm®; Paradigm. <http://www.pdgm.com/products/gocad.aspx> [Accessed July 15, 2014]

Pellerin, J., Botella, A., Mazuyer, A., Chauvin, B., Bonneau, F., Caumon, G., and Levy, B., 2017. RINGMesh: A programming library for developing mesh-based geomodeling applications; Computers & Geosciences, v. 104, p. 93–100. https://doi.org/10.1016/j.cageo.2017.03.005

Schetselaar, E., Bellefleur, G., Craven, J., Roots, E., Cheraghi, S., Shamsipour, P., Caté, A., Mercier-Langevin, P., El Goumi, N., Enkin, R., and Salisbury, M., 2017. Geologically driven 3D modelling of physical rock properties in support of interpreting the seismic response of the Lalor volcanogenic massive sulphide deposit, Snow Lake, Manitoba, Canada; *in* Characterization of ore-forming systems from geological, geochemical and geophysical studies, (ed.) K. Gessner, T.G. Blenkinsop, and P. Sorjonen-Ward; Geological Society of London, Special Publications, v. 453, no. 1, p. 57–79. https://doi.org/10.1144/SP453.5

Shepard, D., 1968. A two-dimensional interpolation function for irregularly-spaced data; *in* Proceedings of the 1968 ACM National Conference; Association for Computing Machinery, New York, New York, p. 517–524. https://doi.org/10.1145/800186.810616

Si, H., 2014. Tetgen: A quality tetrahedral mesh generator and three-dimensional Delaunay triangulator. <http://tetgen.berlios.de>

Yang, D., Fournier, D., Kang, S., and Oldenburg, D.W., 2019. Deep mineral exploration using multi-scale electromagnetic geophysics: the Lalor massive sulphide deposit case study; Canadian Journal of Earth Sciences, v. 56, no. 5, p. 544–555. https://doi.org/10.1139/cjes-2018-0069

Zehner, B., Börner, J.H., Görz,I., and Spitzer, K., 2015. Workflows for generating tetrahedral meshes for finite element simulations on complex geological structures; Computers & Geosciences, v. 79, p. 105–117. https://doi.org/10.1016/j.cageo.2015.02.009

Zhang, P. and Chouteau, M., 1992. The use of magnetotellurics for mineral exploration: an experiment in the Chibougamau region of Quebec; Canadian Journal of Earth Sciences, v. 29, no. 4, p. 621–635. https://doi.org/10.1139/e92-054